Solar cell efficiency divergence due to operating spectrum variation

Geoffrey S. Kinsey

Zuva Energy

Abstract

A limitation in the performance rating of solar cells and modules is that they are tested using a single value for the solar spectrum. To map the performance expected under the varying spectra found in operating conditions, solar cell efficiencies have been evaluated using solar spectra generated by the National Solar Radiation Database, applied to confirmed record-efficiency cell parameters. Nine solar cell types (single-junction and multijunction) are evaluated using spectra at more than forty locations, spanning 76° of latitude and 150° of longitude, at hourly intervals over a year. Relative to the standard test efficiency, increases in annual operating efficiency are seen in cadmium telluride and single-junction perovskite designs, while efficiency decreases are observed in two-terminal multijunction structures. Though silicon exhibits the least variation, its -3% to +2% range in relative efficiency is equivalent to ~20° C of temperature variation. This divergence in operating efficiencies indicates that evaluation using a single spectrum is not a sufficient basis for comparison, or prediction of energy yield in operation. Application of an additional "operating spectrum," to complement the standard test spectrum, is proposed.

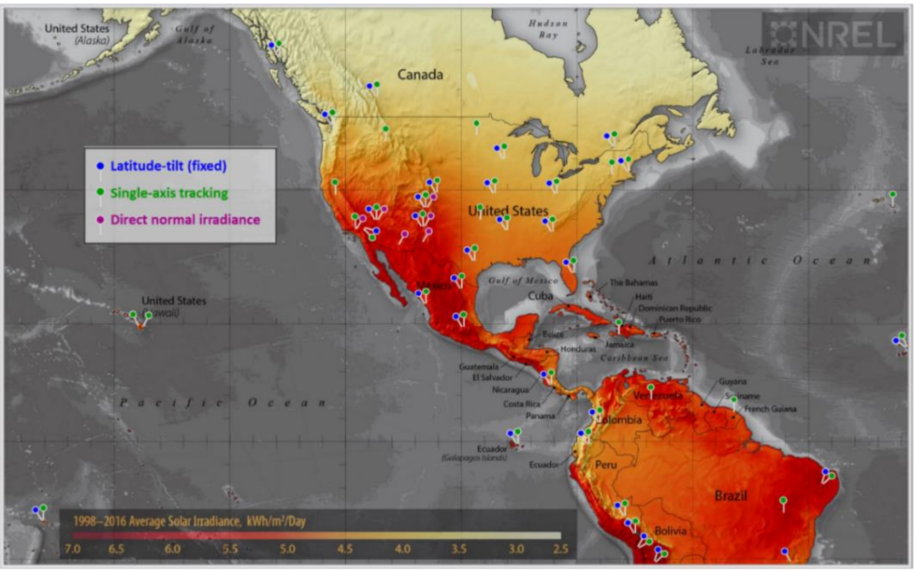

Fig. 1. Source locations for spectra in this study. Each marker represents about 4000 hourly spectra, for wavelengths from 280 nm to 4000 nm. In six locations, hourly spectra were generated for direct normal irradiance (DNI) using inputs from the Typical Meteorological Year 3 database (NREL, 2010) to generate spectra using the SMARTS model (Gueymard, 1995). Map courtesy of NREL's NSRDB.

1. Introduction

While remarkable change has swept across the solar photovoltaics industry in the last four decades, there has been at least one constant: efficiency of cells and modules is determined using a single standard spectrum (ASTM G173-03, 2013; First Solar, 2020; Green et al., 2020a; Green and Emery, 1993; Gueymard et al., 2002; IEC 61215-1, 2016; IEC 61853-2, 2016; Myers et al., 2004, 2002; SunPower, 2020). To obtain repeatable measurements, solar cells and modules are tested under indoor solar simulators that are calibrated to deliver a given irradiance and spectrum (Fraunhofer ISE, 2020; IEC 60904-9, 2006). Use of a single, fixed standard spectrum value has delivered valuable continuity over the years and consistency across academia and industry. Single-value testing cannot, of course, provide insight into the impact of spectrum variation on solar operations worldwide. When comparing devices with different spectral responses for their usefulness in outdoor energy generation, the results of single-spectrum testing, if not representative of operating spectra, are potentially misleading (Amillo et al., 2015; Faine et al., 1991; Lee et al., 2015; Nann and Emery, 1992; Schweiger, 2015). This work maps the impact of operating spectrum variation over a range of latitudes and longitudes and offers a template for determining energy generation for various solar cell types.

2. Synthetic spectra

Synthetic spectra (Fig. 1) have been obtained from the National Renewable Energy Laboratory's (NREL's) National Solar Radiation Database (NSRDB) (Habte et al., 2017; Sengupta et al., 2018). Spectra are generated via the Fast All-sky Radiation Model for Solar applications with Narrowband Irradiances on Tilted surfaces (FARMS-NIT) model (Xie et al., 2019; Xie and Sengupta, 2018). These "global" spectra (including scattered sunlight from the hemisphere of the sky) are generated by the model at hourly intervals for fixed-tilt and single-axis tracking panel orientations (Figure 1). For the fixed-tilt configuration, the site latitude was chosen as the tilt angle. Six hourly "direct" spectra (for sunlight coming directly from the vicinity of the solar disc, derived separately) are also included (Kinsey et al., 2013). The direct spectra are relevant primarily for the III-V multijunctions, which are most often used in optical systems that effectively capture only the direct solar beam (Appendix C). Each dataset (global or direct) represents about 4000 hourly spectra for which the model calculated a non-zero irradiance, with a wavelength range of 280 nm to 4000 nm (Supplemental Table E.1).

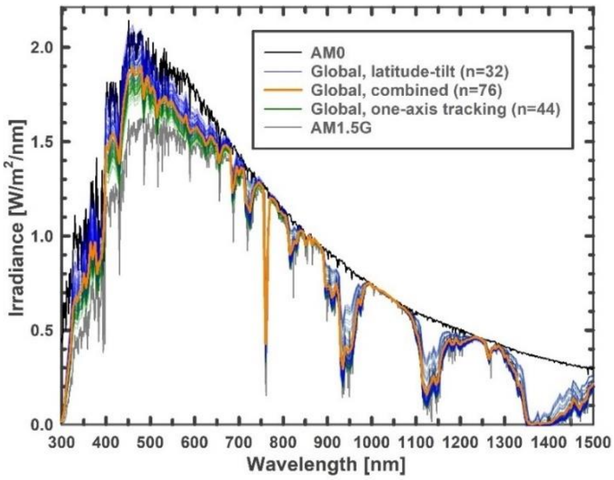

Fig. 2. Annual summations of seventy-six hourly global operating spectra from forty-five locations for NSRDB spectrum year 2018. For comparison with the standard global terrestrial spectrum (AM1.5G, gray) and the standard extraterrestrial spectrum (AM0, black), the global operating spectra amplitudes have been normalized to that of AM0 at 1050 nm.

3. Analysis

Analysis focuses on the global spectra provided by the NSRDB (Fig. 2). Relative to AM1.5G, the annual global spectra exhibit more power density in the visible wavelengths (400-700 nm). Since single-axis trackers follow the sun from/to the horizons, the resulting aggregated spectral content appears less "blue" than for the latitude-tilt (fixed) orientations (Figs. E.1 & E.2).

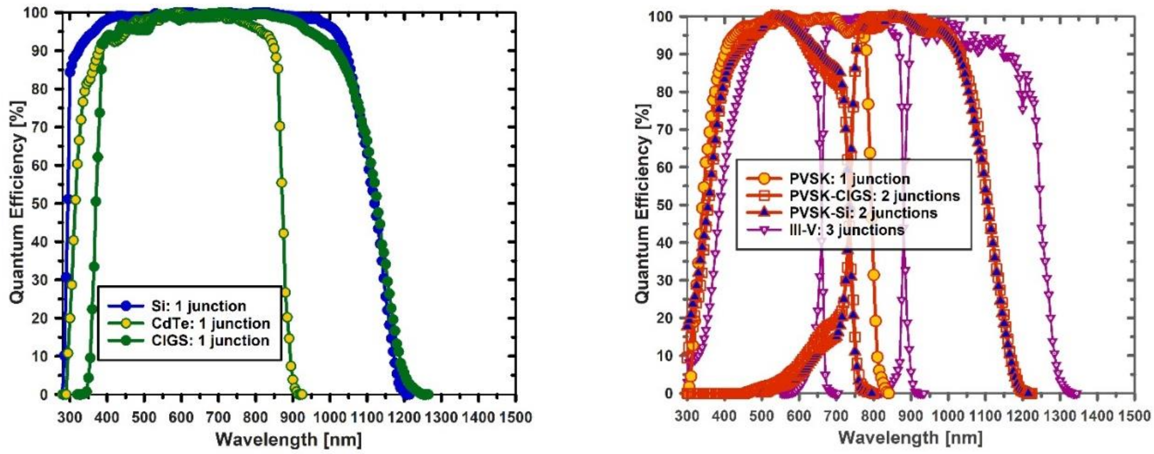

(a) (b)

Fig. 3. Quantum efficiencies for seven of the nine cell types in this study, digitized at 5-nm intervals from figures in the *Solar Cell Efficiency Tables*: (a) silicon (Si), cadmium telluride (CdTe), and CIGS; (b) perovskite (PVSK), perovskite-CIGS tandem (PVSK-CIGS), perovskite-silicon tandem (PVSK-Si) and a III-V three-junction cell. The quantum efficiencies for the III-V four-junction and III-V six-junction cells are shown in Supplemental Fig. E.4.

Performance data for nine confirmed current-best solar cells, chronicled in the *Solar Cell Efficiency Tables* (Green et al., 2020a) and displayed on NREL's Best Research-Cell Efficiency Chart (NREL, 2020), are compared. Four single-junction cells (silicon (Green et al., 2017), cadmium telluride (Green et al., 2015), CIGS (Green et al., 2019), and perovskite (Green et al., 2020b)) are included, as well as five two-terminal multijunctions (perovskite-CIGS (Green et al., 2020a), perovskite-silicon (Green et al., 2020a), and three-, four- and six-junction III-Vs (Green et al., 2019, 2015, 2013). Multijunctions use two or more semiconductor junctions to convert solar energy. Stacking the junctions increases the cell voltage, but the two-terminal configuration implies a series connection, so the device current is limited by whichever junction is producing the least current. Two-terminal multijunctions are therefore more sensitive to spectrum variation.

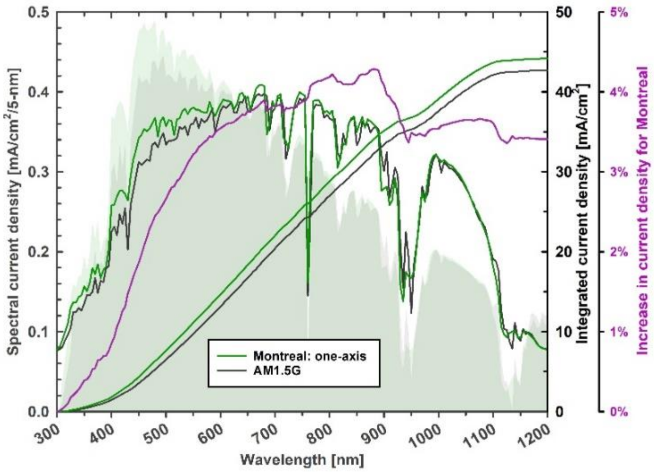

Fig. 4. Current densities for the silicon cell derived from its quantum efficiency combined with spectral irradiances for the standard global spectrum (AM1.5G) and the annual global operating spectrum for single-axis tracking in Montreal. The purple line indicates the relative increase in integrated current density for Montreal with respect to AM1.5G. Spectral irradiances in the background are not shown to scale.

In calculation of the operating efficiencies at 25° C, the open-circuit voltage (V_{OC}) and fill factor (FF) are those confirmed under Standard Test Conditions (IEC 61853-2, 2016, Appendix A). Second-order effects, such as changes to voltage or fill factor with changing irradiance (Kinsey et al., 2008) or increases in fill factor in multijunctions due to current mismatch (Reynolds and Smirnov, 2015) are neglected. Spectrum variations (and their integral, the irradiance) are assumed to affect only the cell short-circuit current. The short-circuit current is derived from a cell's quantum efficiency, which is a measure of the percentage of incoming photons at each wavelength that are converted by a solar cell into current. Quantum efficiencies provided in the *Solar Cell Efficiency Tables* are digitized at 5-nm wavelength intervals (Fig. 3). Since the amplitude of the published quantum efficiencies is often normalized, the amplitudes are re-normalized to deliver the short-circuit current confirmed under the standard spectrum, AM1.5G (AM1.5D, for the III-V multijunctions, Appendix B).

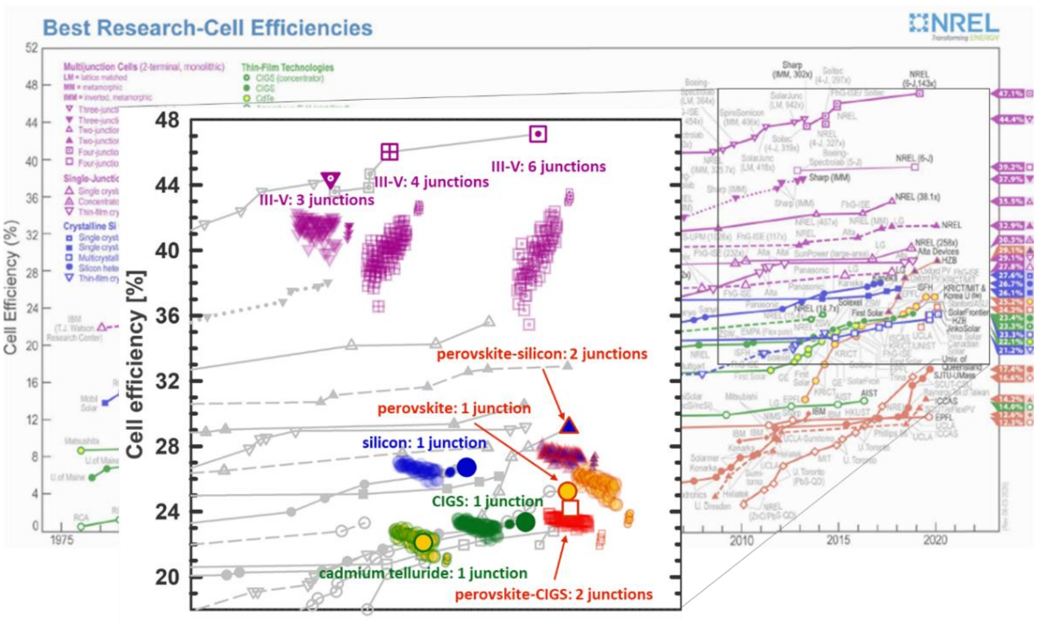

Fig. 5. Annual operating efficiencies under variable operating spectra at 25° C, compared against the values under Standard Test Conditions ("STC", largest icons: 25° C, 1000 W/m^2, and AM1.5G or AM1.5D spectrum, Appendix A). Symbols for operating spectra are arranged in order of increasing annual site irradiance; lateral positions are adjusted to improve visibility. The rightmost data (smallest symbols, separated by a gap) are for the six direct normal irradiance datasets. Best Research-Cell Efficiency chart courtesy of NREL (NREL, 2020).

To determine the short-circuit current under a given spectrum, the hourly spectra are converted to 5-nm intervals, to pair with the digitized quantum efficiencies. Fig. 4 illustrates the relationship between spectral irradiance and a cell's spectral current density. Spectral current density is integrated across all wavelengths to give the short-circuit current density, J_{SC} [A/cm^2]. The product $V_{OC}\cdot FF\cdot J_{SC}$ is then the cell power density [W/cm^2]. Dividing by the irradiance [W/cm^2] gives the efficiency.

Resulting annual operating efficiencies (at 25° C) are shown in Fig. 5, against a backdrop of the confirmed values under AM1.5G (AM1.5D, for the III-V multijunctions). The corresponding relative efficiencies are given in Fig. 6. While the efficiencies for silicon and CIGS are clustered around their values under the standard spectrum, those of the other cell types diverge. Cadmium telluride and the single-junction perovskite deliver higher efficiencies at most locations, while the multijunctions deliver lower. As might be expected, sensitivity to spectrum variation increases with the number of junctions, leading to decreased efficiency and greater variation between locations. Researchers recognize this limitation of two-terminal (series-connected) multijunctions; the search for practical three- or four-terminal alternatives is underway (Futscher and Ehrler, 2017).

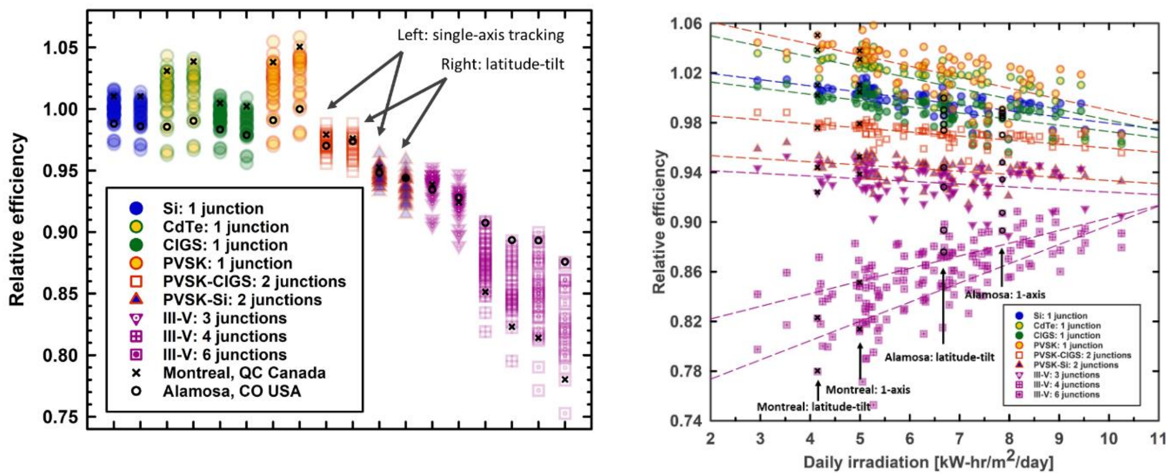

(a) (b)

Fig. 6. Efficiencies under annual global spectra at 25° C, relative to that confirmed under a standard spectrum. Data grouped by cell type in (a) is shown as a function of site daily irradiation in (b). Linear regressions to the data are included in (b) solely as guides to the eye. Abbreviations: silicon (Si); cadmium telluride (CdTe); perovskite (PVSK).

Two locations, Montreal, Canada and Alamosa, USA, are highlighted in Fig. 6 to illustrate the varying impact of given spectral conditions on different cell designs: as cell spectral sensitivity increases from left to right in Fig. 6(a), the higher efficiencies found in Montreal (for single-junctions) shift to Alamosa (for multijunctions). Efficiencies as a function of site latitude are given in Fig. E.7.

Relative to silicon, the higher efficiency of cadmium telluride and single-junction perovskite is notable in sites like Montreal. It can be understood with reference to the integrated current density in Fig. 4, obtained by summing the spectral current density in the direction of increasing wavelength. Examination of Fig. 3 shows that quantum efficiency goes to zero above 840 nm for single-junction perovskite and 915 nm for cadmium telluride, while for silicon it extends to 1200 nm. The increase in integrated current density for silicon in Montreal (with respect to AM1.5G) is 4.1% at 840 nm, 3.9% at 915 nm, but drops to 3.4% at 1200 nm. The peak benefits are therefore with the perovskite and cadmium telluride cells, while silicon receives a lower proportional benefit. The 3.4% gain in current density for silicon is partly offset by a corresponding rise in irradiance (2.4%, not shown) for a net efficiency gain of 1.0%, relative.

Divergence in cell response under spectrum variation is further evident when plotted as a function of irradiance in Fig. 6(b). The atmospheric conditions that determine spectrum at the surface are complex, so a simple linear relationship between cell efficiency and site irradiation is not expected. However, site conditions are frequently covariant; a dry, high-altitude site such as Alamosa, USA will often have fewer clouds, fewer aerosols, and less water in the atmosphere. Across the highland plateaus of South America, spectra can approach the shape of the extraterrestrial spectrum (Fig. E.9). In contrast, lower daily irradiance levels in sites such as Montreal often imply a wider range of atmospheric conditions that leads to larger divergences in the spectra and the cell efficiencies in both seasonal and hourly timescales (Figs. E.1, E.2, E.3).

The output files from the NSRDB include hourly ambient temperature, so temperature corrections to open-circuit voltage, fill factor, and the short-circuit current densities are applied (using temperature coefficients in Table E.2). Table 1 includes annual summaries of the spectrum- and temperature-corrected data. For single junctions, the effects of operating spectral variation are comparable in magnitude to the effects of temperature. Silicon shows the least sensitivity to spectral variation, yet its ~5% variation range at 25° C (-3% to +2%) is equivalent to 20° C of temperature excursion. For cadmium telluride, which exhibits larger spectral variation and has a smaller temperature coefficient, the ~8% variation range is equivalent to over 30° C of temperature excursion.

Table 1. Efficiency under standard test conditions (η_{STC}), operating spectra at 25° C ($\eta_{25°C}$), and operating spectra and temperature (η_T).

Cell (junctions)	η_{STC} [%]	$\eta_{25°C}$ [%]	median $\eta_{25°C}$		$\frac{\eta_{25°C} - \eta_{STC}}{\eta_{STC}}$	η_T	$\frac{\eta_T - \eta_{STC}}{\eta_{STC}}$
			1-axis	lat.-tilt			
Silicon (1)	26.7	25.8-27.1	26.7	26.7	-3% to +2%	24.5-26.5	-8% to -1%
CdTe (1)	22.1	21.3-23.1	22.5	22.5	-4% to +4%	20.8-22.5	-6% to +2%
CIGS (1)	23.4	22.3-23.6	23.2	23.1	-5% to +1%	20.9-23.0	-11% to -2%
PVSK (1)	25.2	24.5-26.7	25.8	25.9	-3% to +6%	23.8-25.9	-5% to +3%
PVSK-CIGS (2)	24.2	23.0-23.9	23.5	23.5	-5% to -1%	21.2-23.4	-12% to -3%
PVSK-Si: (2)	29.2	26.7-28.1	27.6	27.4	-9% to -4%	24.8-27.5	-15% to -6%
III-V (3)	44.4	39.5-42.3	41.7	41.2	-11% to -5%	39.0-41.9	-12% to -6%
III-V (4)	46.0	36.6-41.8	40.3	39.6	-20% to -9%	35.7-41.1	-22% to -11%
III-V (6)	47.1	35.5-42.4	40.1	39.2	-25% to -10%	34.6-41.4	-27% to -12%

If not accounted for, such variation leads to miscalculations of solar power generation capability that impact project economics and climate change mitigation. For a notional 100-MW solar project commissioned at €1/W, generating 1500 kWh/kW/year and selling into the electrical grid at €0.05/kWh, a 2% difference between predicted and actual output translates to a project cost difference of €2 million and an annual revenue difference of €150,000. If this solar plant displaces fossil fuel generating carbon dioxide at 0.5 kg/kWh (Foster and Bedrosyan, 2014), the annual difference in greenhouse gases would be 1,500 tons in the first year, the equivalent of around 9 flights from New York to Paris (Air Transport Action Group, 2020, Appendix D).

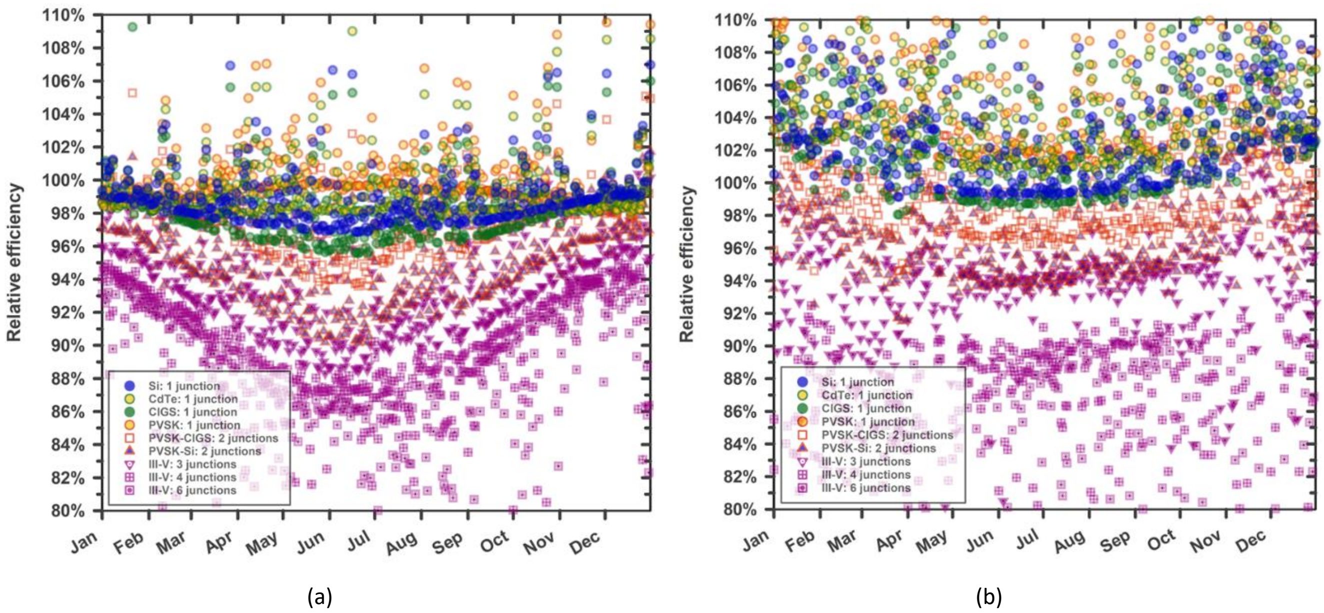

Fig. 7. Daily relative efficiencies at 25° C for Alamosa, USA (latitude-tilt) and Montreal, Canada (one-axis tracking). Results for other sites are in Table E.4.

The value of solar to the grid depends on the season and time of day that it is generated. The hourly granularity of NSRDB spectral irradiance outputs enables investigation of these variations (Fig. 7, Table E.4, Fig. E.3). Along with the greater daily fluctuations seen in the Montreal climate, there are also differences in the curvatures of cell efficiency due to seasonality. The seasonal curvatures of silicon, cadmium telluride, and CIGS cells are more pronounced in Montreal; the May-August peak seen in the performance of the perovskite single junction in Alamosa is more of a trough in Montreal. Seasonal variation of silicon and cadmium telluride across multiple sites is shown in Fig. E.8.

4. Discussion

In 1992, Keith Emery of NREL, ever a champion of rigorous testing standards, co-authored a paper addressing the many discrepancies between then-standard testing and outdoor performance. Regarding spectrum, the authors observed:

> …There are changes in the relative spectral distribution which lead to higher or lower efficiencies compared to the efficiency under the AM1.5 reference spectrum… With a few exceptions, all PV-modules have been overrated because the single-value specification of efficiency under standard reporting conditions is a more favorable specification than that measured outdoors under real conditions. This discrepancy, however, should occur between measurements and rating, but not between rating and customer. (Nann and Emery, 1992)

In the decades since, multiple values for other factors that affect performance (temperature, irradiance, wind speed, e.g.) have been standardized and incorporated into test protocols, product data sheets (First Solar, 2020; Solar Frontier, 2020; SunPower, 2020), and warranty coverage terms (Jinko Solar, 2020), so that the link between standard testing and outdoor operation is understood. Use of a single spectrum has become the outlier.

Today's international standard for energy rating of photovoltaic modules (IEC 61853-2, 2016) defines four temperatures, four irradiances… And one spectrum. An impediment to defining additional "operating spectra," consistent with what is now required for temperature and irradiance, has been the uncertainty around what those operating spectra should be. Results presented here and in the literature (Alonso-Abella et al., 2014; Amillo et al., 2015; Cornaro and Andreotti, 2013; Dirnberger et al., 2015; Faine et al., 1991; Fernandez et al., 2015; Gottschalg et al., 2004; Huld and Gracia Amillo, 2015; Ishii et al., 2013; Kinsey et al., 2013; Kinsey, 2015; Lee et al., 2015; Marzo et al., 2017; Minemoto et al., 2007; Monokroussos et al., 2011; Nann and Emery, 1992; Peters and Buonassisi, 2018; Philipps et al., 2010; Schweiger, 2015; Simon and Meyer, 2011; Ye et al., 2014) indicate that this concern is subordinate to the uncertainty arising from reliance on testing under a single-value standard spectrum. Any additional standard spectrum will convert the existing single-value specification into a performance range that, however limited, will enable interpolation and/or extrapolation to conditions of interest to the "customer".

One candidate for a "standard operating spectrum" might be something like the composite of seventy-six annual spectra shown in Fig. 2. However, two other candidates are already qualified as standards and can therefore be implemented immediately: AM1.5D (ASTM G173-03, 2012) and AM0 (ASTM E490-00a, 2014). While AM0, the standard for space (Fig. C.1), would be an extreme choice in terms of representing terrestrial spectra (Fig. E.6, Table E.3), AM0 paired with AM1.5G would bracket most operating spectral conditions worldwide and serve as a lower bound for predicting cell and module operating efficiencies.

Conclusion

Nine cell types have been evaluated under operating spectra obtained from the National Solar Radiation Database. The resulting variation in cell operating efficiencies is comparable to that resulting from temperature variations. Efficiencies diverge for cells with different spectrum sensitivities, so testing under more than a single spectrum is indicated for comparison and energy yield prediction. Implementation of one or more standard operating spectra, to supplement the standard test spectrum, will reduce uncertainty in the costs and benefits in deploying solar photovoltaics.

Appendix A: methods

Synthesized spectra

Sophisticated models for solar spectral irradiance have been developed to enable synthesis of spectral using input atmospheric conditions. Inputs include site pressure and aerosol, water vapor, ozone, and CO_2 levels. The outputs are corroborated with a growing body of measurements from both satellite (NOAA/NASA GOES-R) and ground-based spectroradiometer data. The National Solar Radiation Database at NREL hosts *Spectral On-Demand*, a tool accessible online as part of the satellite-derived data in the NSRDB Data Viewer. *Spectral On-Demand* generates synthetic spectra for points within the area defined by NREL's Physical Solar Model: longitude: -25°E to -175°W, latitude: -20°S to 60°N). Spectrum data is generated at one-hour intervals using the Fast All-sky Radiation Model for Solar applications with Narrowband Irradiances on Tilted surfaces (FARMS-NIT. Within FARMS-NIT, clear-sky irradiance is first calculated using SMARTS (Simple Model of the Atmospheric Radiative Transfer of Sunshine) (Gueymard, 1995; Myers and Gueymard, 2004). SMARTS has demonstrated predictive power for the operation of spectrum-sensitive solar cells (Kinsey et al., 2013). A version of SMARTS (v. 2.9.2) is the basis for defining the current American Society for Testing and Materials standards for AM1.5G and AM1.5D (ASTM G173-03), as well as the International Electrotechnical Commission (IEC) standard for AM1.5 (IEC 60904-03). The NSRDB spectrum year used here is 2018.

For direct normal irradiance, the Typical Meteorological Year 3 database (NREL, 2010), a predecessor to NREL's Physical Solar Model, was used for inputs to the SMARTS model.

Standard Test Conditions

Standard Test Conditions (STC) require a 25° C cell temperature, 1000 W/m^2 irradiance, and the AM1.5G spectrum for cells and modules. An exception is made for components under optical concentration and using the ASTM standard (III-V multijunctions, e.g.), for which the irradiance is 900 W/m^2 and the spectrum is AM1.5D.

Standard operating conditions are defined for sets of temperature and irradiance. An example is IEC 61853, "Photovoltaic (PV) module performance testing and energy rating":

Table A.1. Standard test conditions per IEC 61853.

	Irradiance	Temperature (point of reference)	Spectrum
Standard Test Conditions	1000 W/m^2	25° C (cell)	AM1.5
Nominal Operating Cell Temperature	800 W/m^2	20° C (ambient)	AM1.5
Low Irradiance Condition	200 W/m^2	25° C (cell)	AM1.5
High Temperature Condition	1000 W/m^2	75° C (cell)	AM1.5
Low Temperature Condition	500 W/m^2	15° C (cell)	AM1.5

The "AM1.5" spectrum in IEC 61853 is defined in IEC 60904-03 and is consistent with (though not quite identical to) AM1.5G, as defined by ASTM G173-03.

Quantum efficiency and calculation of current density

Quantum efficiencies are measured under short-circuit conditions, where the cell is expected to produce the maximum amount of current. To obtain the current generated under a given spectrum, the spectral irradiance is divided by the photon energy at each wavelength to give the number of photons in that interval (5-nm intervals were used in this study). Multiplying by the quantum efficiency gives the "spectral current density" [mA/cm^2/nm] that would be converted to current at that wavelength. Multiplying by the wavelength interval yields current density [mA/cm^2] for each interval; integrating over all wavelengths obtains the short-circuit current density.

Appendix B: standard spectra

Three standard spectra are in use for space and terrestrial solar applications: AM0, AM1.5D, and AM1.5G. "AM" is short for "air mass" and represents the hypothetical column of air between the sun and the incident surface. AM0 (defined in 1974), is used for solar cells under extraterrestrial radiation, in earth orbit above the atmosphere (zero air mass). An air mass of one ("AM1") would represent the conditions when the sun is directly overhead. When a standard for the terrestrial spectrum was first established by the American Society for Testing and Materials (ASTM) in 1982, AM1.5 was selected to represent a "typical" solar module tilted at a fixed angle of 37° (mid-latitude USA) and pointed due south. The geometry of AM1.5 implies a sun zenith angle of 48.2°. For forty-four sites with one-axis tracking data, the annual, irradiance-weighted zenith angles were obtained (Table E.1); the median irradiance-weighted sun zenith angle for this group is 46.6°.

AM1.5D is the ASTM "direct" spectrum for this orientation, intended to represent only the sunlight coming directly from the sun (or its near vicinity). AM1.5D finds practical application in systems using two-axis trackers and optical concentration (lenses or mirrors) to boost solar cells' power and efficiency. These optical concentrators are effective in concentrating only the collimated rays that come directly from the solar disc. The "global" spectrum, AM1.5G, consists of these direct rays, as well as sunlight that has been scattered by the atmosphere and is arriving on the tilted surface from the hemispherical dome of the sky. Though solar panels in 2020 are at least as likely to be found on trackers as on fixed racks (and even more likely to be installed remote from 37° northern latitudes), use of AM1.5G has remained the convention throughout academia and industry.

Appendix C: III-V multijunctions & global vs. direct normal irradiance

Direct spectra are relevant for solar systems using optical concentration and two-axis tracking; these systems typically employ III-V multijunction cells. The trend in III-V multijunction efficiencies notable in Fig. 5, where the efficiencies in the global spectra rise (or, in the case of the three-junction, fall) to approach those for the direct spectra, is consistent with their design. III-V multijunctions are tuned by their designers for operation under a direct spectrum (AM1.5D).

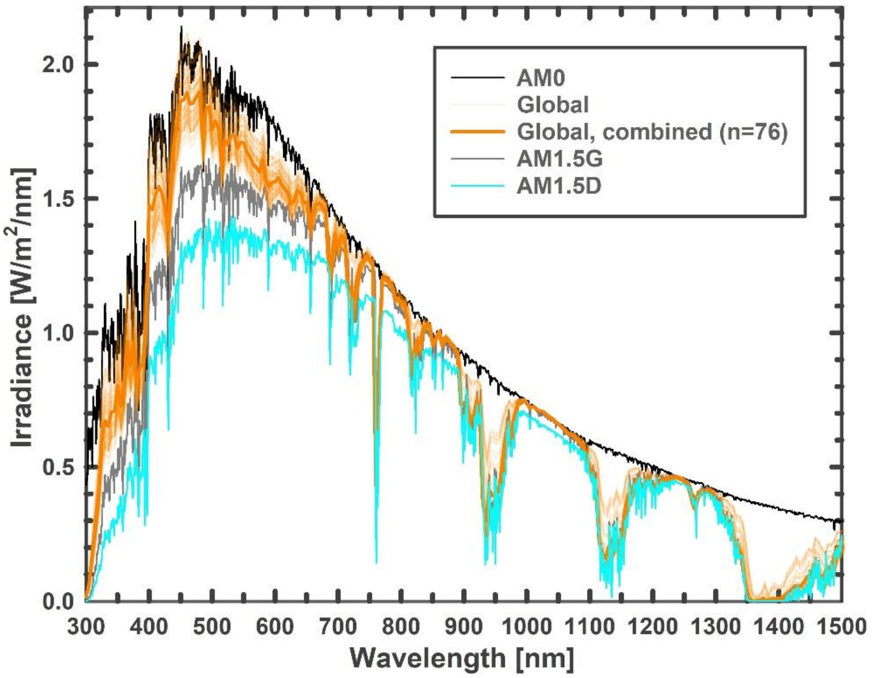

Fig. C.1. Three standard spectra (AM0, AM1.5D, and AM1.5G) compared against seventy-six annual global spectra (one-axis and latitude-tilt) derived from the National Solar Radiation Database (NSRDB) hourly spectra, converted to 5-nm wavelength intervals. The NSRDB global spectra are normalized to the AM0 value at 1050 nm.

Appendix D: estimates of greenhouse gas equivalents in air travel

A Boeing 787-9 carries up to 289 passengers (Boeing, 2020) and consumes approximately 2.9 litres of jet fuel per 100 km per passenger once it is at cruising altitude (Lufthansa, 2020). The 5,800-km trip from Paris to New York will consume approximately 50,000 litres. A litre of jet fuel weighs about 0.8 kg and produces 3.2 kg of CO_2 (Air Transport Action Group, 2020). One-hundred and sixty tons is released for one trip between New York and Paris (0.5 tons per passenger, 83 kg per passenger per hour on a full flight).

Appendix E: supplemental data

Table E.1. Site details: annual values for NSRDB year 2018.

			One-axis tracking		Latitude-tilt		Direct normal	
Location	Temp. [° C] (Irradiance-weighted*)	Sun zenith angle [°] (Irradiance-weighted*)	Daily irradiation [kW-hr/m^2/day]	# of spectra	Daily irradiation [kW-hr/m^2/day]	# of spectra	Daily irradiation [kW-hr/m^2/day]	# of spectra
Azores-Ponta Delgada	17.0	48.9	5.1	4137				
Bolivia-Uyuni	14.0	44.9	10.3	4110	8.0	4110		
Brazil-Mariana			5.1	4207				
Brazil-Patos	32.3	41.1	9.0	4299	5.1	4137		
Brazil-Sao Desiderio	30.1	42.1			8.4	4183		
Cabo Verde-Praia	23.1	41.6	8.4	4156	6.9	4153		
Canada-Calgary	14.8	54.6	4.9	4032	4.2	3878		
Canada-Montreal	15.1	51.8	4.1	4010	5.0	4102		
Chile-Putre	15.4	43.8	9.5	4109	8.0	4222		
Colombia-Cali	24.7	39.0	6.3	4067	5.4	4066		
Costa Rica-Punta Arenas	30.7	39.8	7.5	4208	6.3	4182		
Ecuador-Galapagos	24.0	42.7	6.7	4036	5.3	4036		
Ecuador-Quito	15.5	39.9	5.3	4171	6.3	4171		
French Guiana-Kourou	27.9	39.5	7.3	4249	8.4	4183		
Haiti	22.6	45.3	6.7	4201				
Mexico-Mazatlan	28.9	43.7	8.2	4179	6.8	4159		
Mexico-Mexico City	22.4	41.5	7.6	4138	6.5	4138		
Mexico-Monterrey	30.7	43.4	6.6	4178	5.5	4133		
Peru-Cusco	12.9	42.1	6.9	4171	4.4	3969		
Peru-Puno	13.3	42.7	8.9	4123	7.3	4123		
Samoa-Apia	25.4	41.7	9.4	4174	7.6	4174		
USA-AK-Ketchikan	13.4	55.9	3.5	4013	2.9	3928		
USA-AR-Little Rock	23.9	47.7	5.1	4058	6.2	4127		
USA-AZ-Tucson							9.2	4426
USA-CA-Joshua Tree	24.4	49.0	8.9	4140	7.3	4028		
USA-CA-Palmdale	26.4	48.8	8.6	4117			8.8	4457
USA-CA-Sacramento	25.2	49.6	7.4	4139				
USA-CO-Alamosa	17.3	50.1	7.9	4119	6.7	4066	9.9	4259
USA-CO-Denver	20.5	50.7	6.7	4140	5.8	4076		
USA-FL-Cocoa	25.9	46.1	7.0	4178	6.3	4171		
USA-GA-Atlanta	22.9	47.0	5.2	4121	6.3	4182		
USA-HI-Hilo	27.9	40.7	5.0	4137				
USA-HI-Kona	23.6	45.7	5.1	4140				
USA-MA-Boston	16.6	51.0	5.2	4105	4.4	3969		
USA-MN-Rochester	15.3	52.1	5.3	4124	4.4	4015		
USA-MO-Kansas City	21.9	49.7	5.9	4138	4.9	4026		
USA-MT-Butte	14.5	52.9	5.7	4090				
USA-ND-Fargo	17.1	52.4	5.2	4079	6.3	4157		
USA-NM-Albuquerque	23.8	48.7	8.2	4112	6.8	4052	9.2	4433
USA-NM-Las Cruces							9.2	4429
USA-NV-Las Vegas	29.1	49.4	8.3	4157	6.8	4028	9.0	4307
USA-NY-New Paltz	17.4	50.5	5.0	4148	5.0	4102		
USA-OH-Xenia	19.3	48.9	5.1	4123	4.2	4038		
USA-OK-Yale	23.6	48.5			6.3	4157		
USA-TX-Austin	28.1	45.4	6.6	4211	5.4	4109		
USA-WA-Seattle	17.9	51.9	5.0	4088	4.2	3998		
Venezuela-Apure	31.2	41.0			8.0	4222		

*The irradiance used is the one-axis tracking irradiance.

Alamosa (latitude-tilt) & Montreal (one-axis tracking) data:

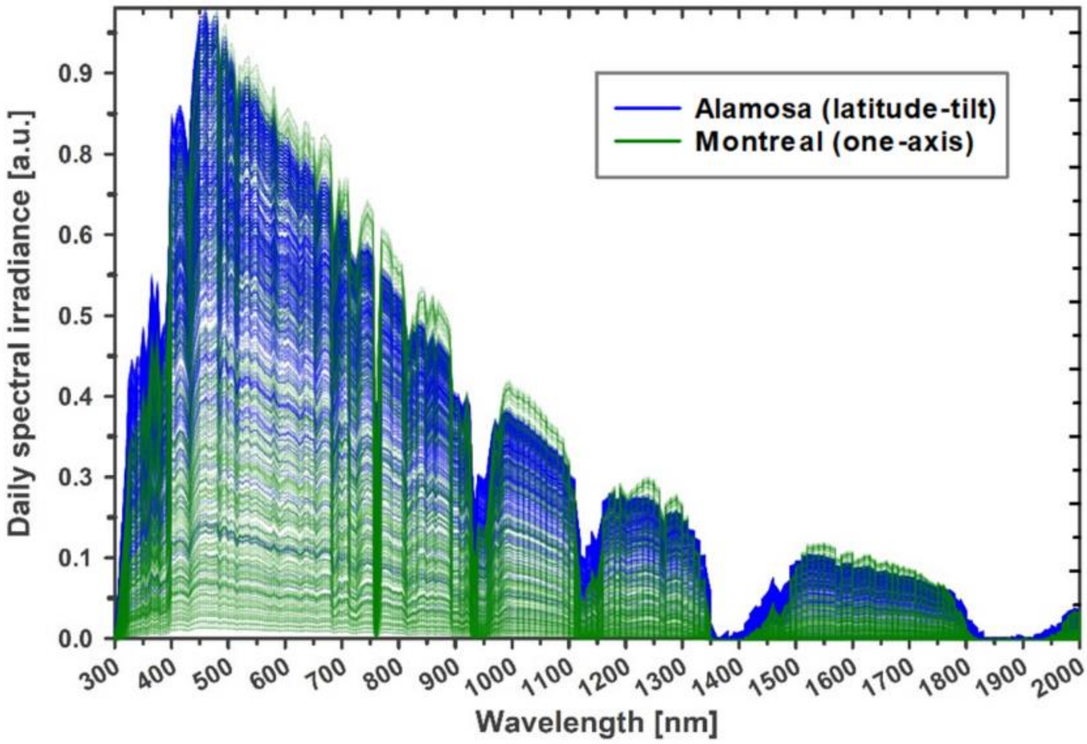

Fig. E.1. Daily spectral irradiances for Alamosa (latitude-tilt) and Montreal (one-axis tracking). Amplitudes are normalized to the peak at each respective location.

Hourly data on the summer solstice in Alamosa, USA and Montreal, Canada

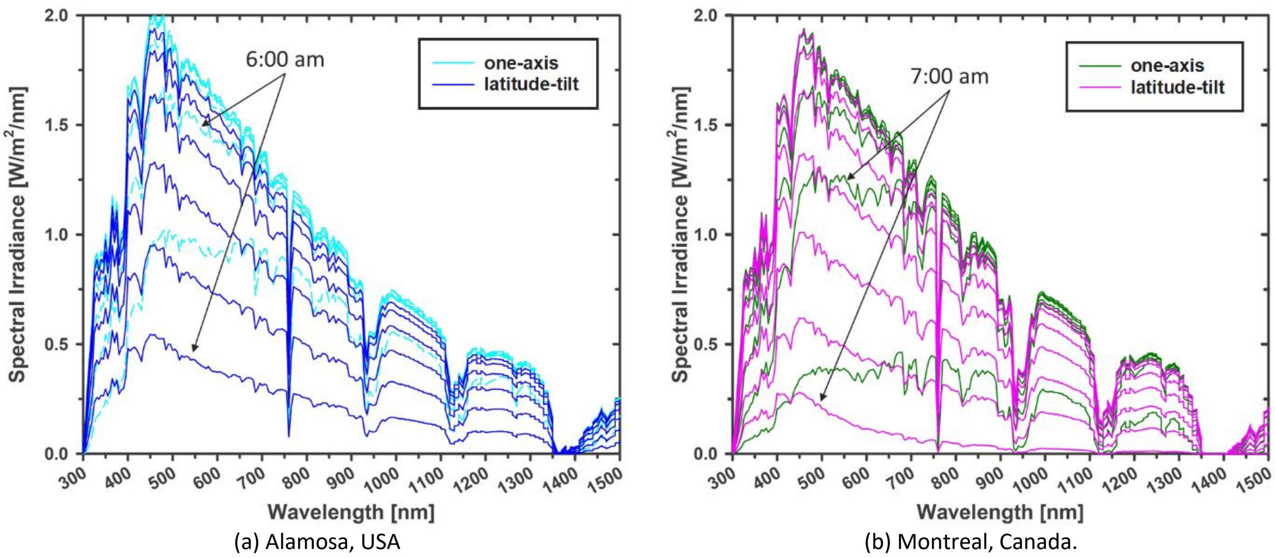

(a) Alamosa, USA (b) Montreal, Canada.

Fig. E.2. Morning hourly spectra (up to the peak daily irradiance, near solar noon) on the summer solstice (21 June 2018). For the latitude-tilt orientation, the first non-zero spectrum is at 6:00 am in Alamosa and 7:00 am (local time) in Montreal.

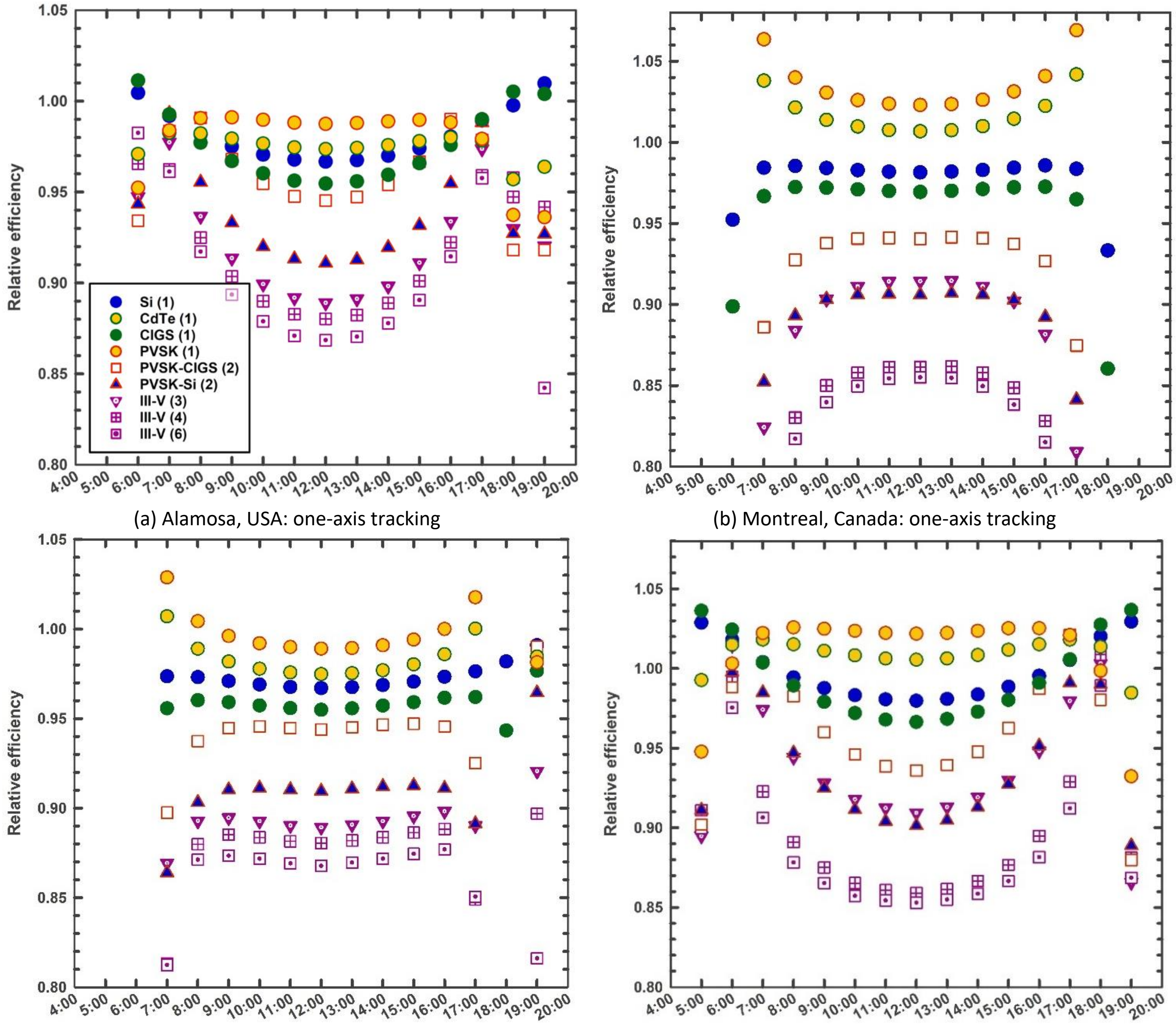

(a) Alamosa, USA: one-axis tracking (b) Montreal, Canada: one-axis tracking

(c) Alamosa, USA: latitude-tilt (d) Montreal, Canada: latitude-tilt

Fig. E.3. Relative efficiencies at 25° C on the summer solstice (21 June 2018) as a function of local time.

Quantum efficiencies

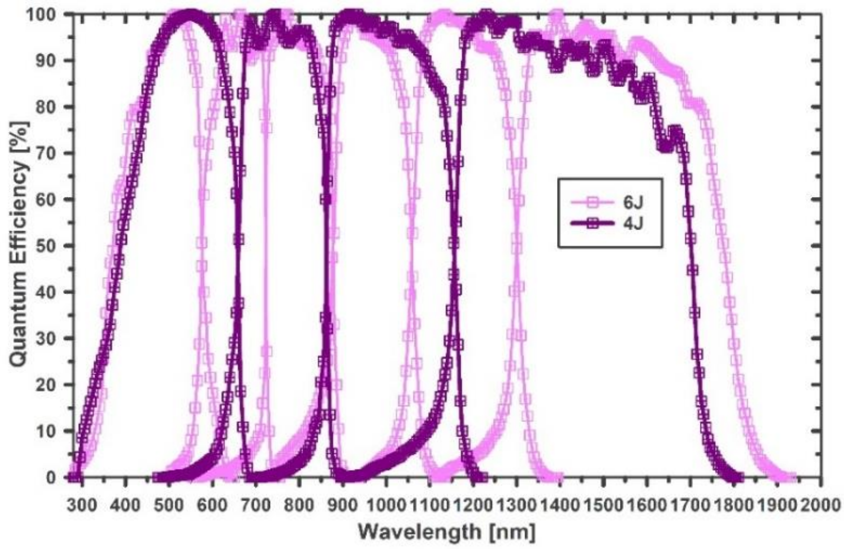

Fig. E.4. Quantum efficiencies of the III-V four- and six-junction cells (Green et al., 2019, 2015).

Efficiencies under operating spectra and temperatures:

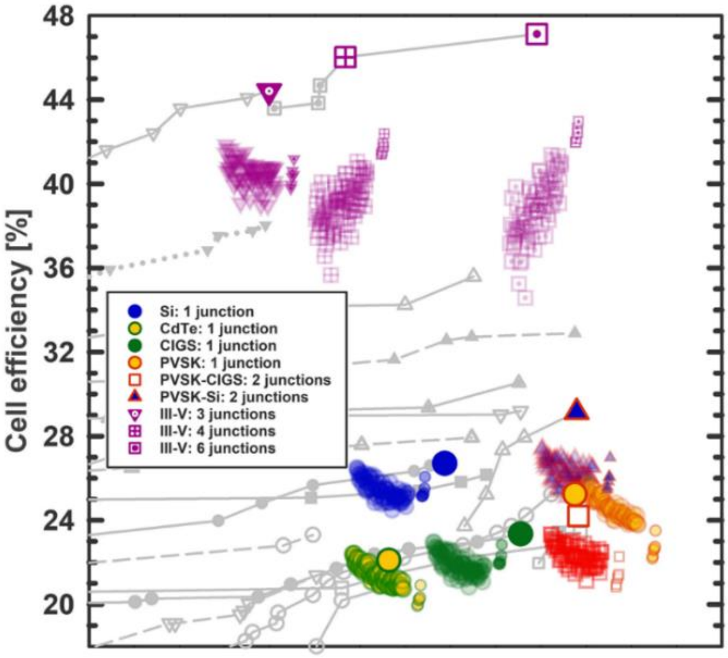

Fig. E.5. Efficiencies under operating spectra and temperatures.

Efficiencies under operating spectra, AM1.5G, AM1.5D, and AM0

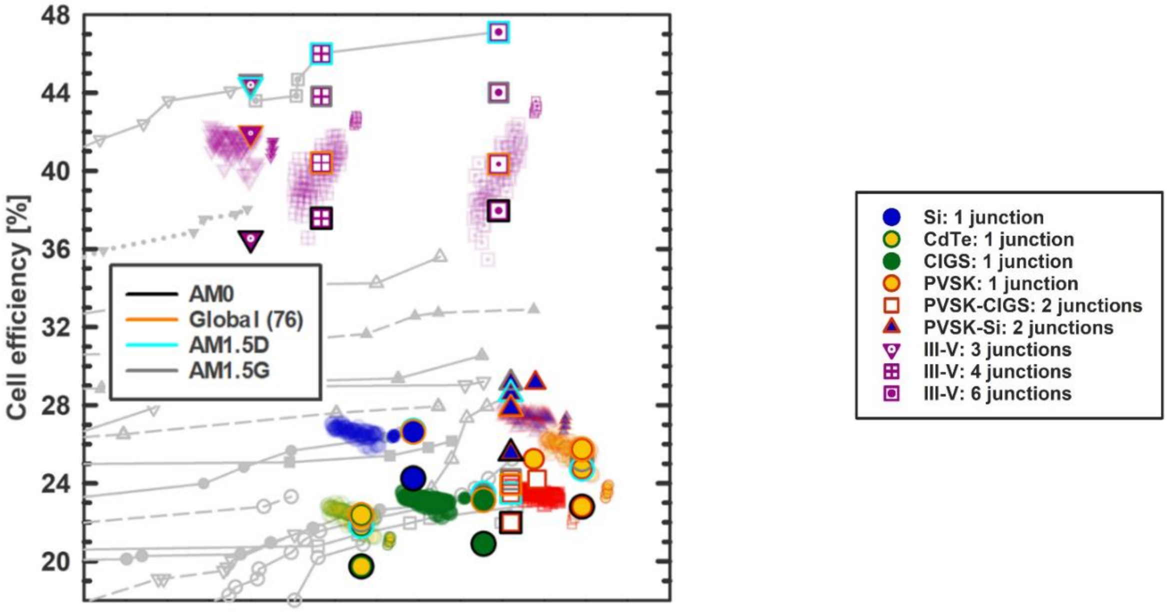

Fig. E.6. Efficiencies under operating spectra (at 25° C), AM1.5G, AM1.5D, and AM0. Some lateral positions are adjusted to improve visibility.

Table E.3. Efficiencies under three standard spectra (at 25° C).

Cell (# junctions)	AM0	AM1.5G	AM1.5D
Silicon (1)	24.2%	26.7%	26.7%
CdTe (1)	20.9%	23.4%	23.5%
CIGS (1)	19.7%	22.1%	21.8%
PVSK (1)	22.8%	25.2%	24.7%
PVSK-CIGS (2)	22.0%	24.2%	23.5%
PVSK-Si: (2)	25.5%	29.2%	28.6%
III-V (3)	36.5%	44.6%	44.4%
III-V (4)	37.6%	43.8%	46.0%
III-V (6)	38.0%	44.0%	47.1%

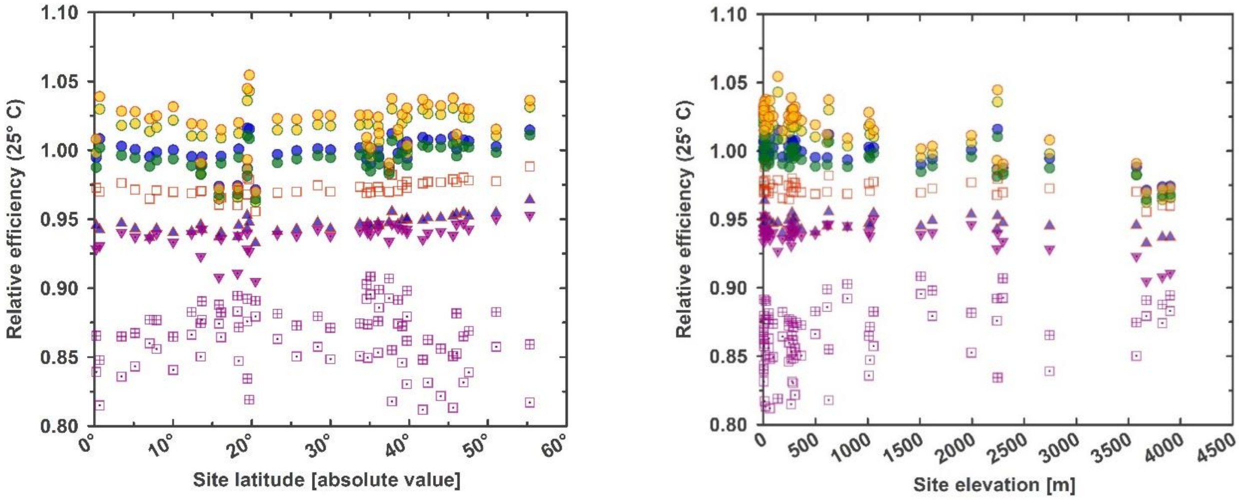

(a) (b)

Fig. E.7. Relative efficiency (at 25° C) under annual operating spectra (global, one-axis tracking) as a function of (a) site latitude and (b) site elevation.

Cell parameters

Table E.2. Cell parameters used in efficiency calculations.

Cell (# junctions)	Si (1)	CdTe (1)	CIGS (1)	PVSK (1)	PVSK-CIGS (2)	PVSK-Si (2)	III-V (3)	III-V (4)	III-V (6)
V_{oc} (25° C)	0.738	0.8872	0.734	1.1805	1.897	1.768	3.555	4.23	6.286
FF (25° C)	0.849	0.785	0.804	0.848	0.778	0.729	0.872	0.85	0.872
dV_{OC}/dT [%/°C]	-0.00241	-0.0027	-0.00300	-0.0012	-0.00167*	-0.0020*	-0.00135	-0.00135	-0.00135
dI_{SC}/dT [%/°C]	0.00055	0.0004	0.0001	-0.00054	-0.00012*	-0.00027*	0.0006	0.0006	0.0006
dFF/dT [%/°C]	-0.00072	-0.0002	-0.000020	-0.00094	-0.00086*	-0.00063*	-0.00053	-0.00053	-0.00053
dP/dT [%/°C]	-0.00258	-0.0025	-0.0031	-0.0027	-0.0026*	-0.0029*	-0.0013	-0.0013	-0.0013

*The temperature coefficients of perovskites are not yet well understood; the temperature coefficient for perovskite fill factor was taken as a mean from the range of values shown in the supplement to Jošt et al., 2020. Temperature coefficients for PVSK-CIGS and PVSK-Si are calculated as the V_{OC}-weighted averages of the coefficients of the two materials.

Values for the open-circuit voltage (V_{OC}) and fill factor (FF) are found in Green et al., 2020a. The sources for temperature coefficients are: silicon (SunPower, 2020); cadmium telluride (First Solar, 2020); CIGS (Solar Frontier, 2020); perovskite (Jošt et al., 2020); III-Vs (Fernández et al., 2012)

Table E.4. Select daily efficiencies (global & direct spectra, 25° C).

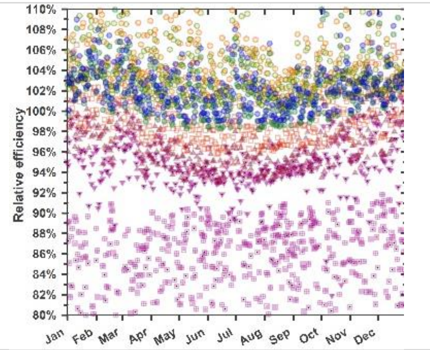

Azores-Ponta Delgada (one-axis tracking)

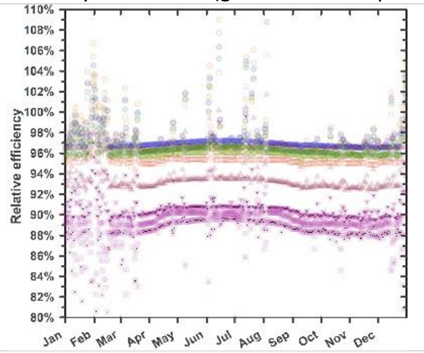

Bolivia-Uyuni (one-axis tracking)

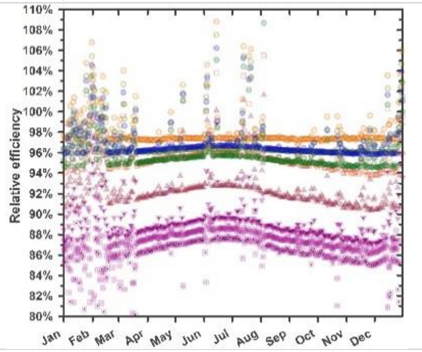

Bolivia-Uyuni (latitude-tilt)

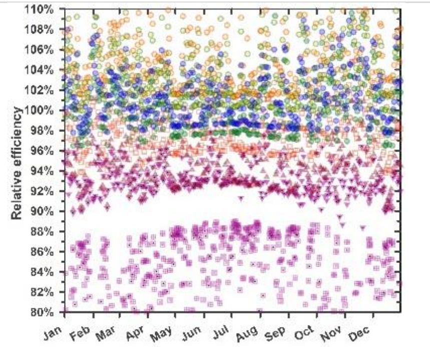

Brazil-Mariana (latitude-tilt)

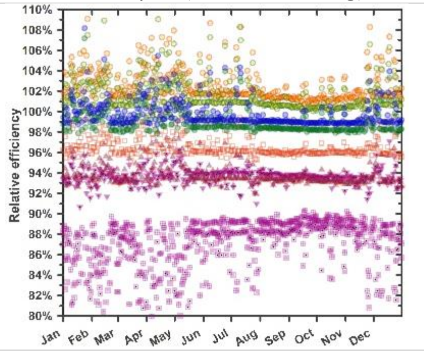

Brazil-Patos (one-axis tracking)

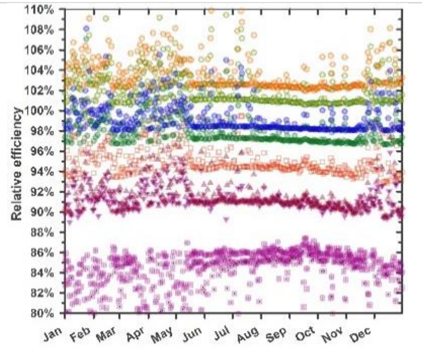

Brazil-Patos (latitude-tilt)

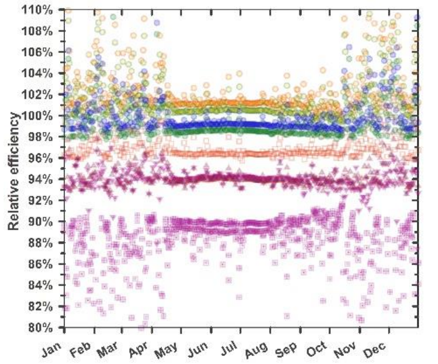

Brazil-Sao Desiderio (one-axis tracking)

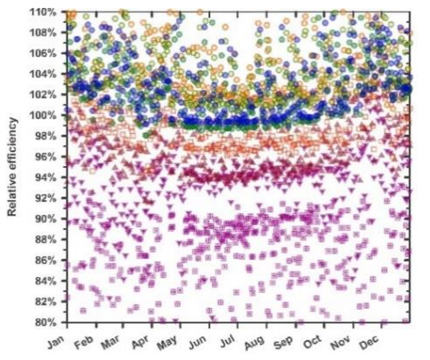

Canada-Montreal (one-axis tracking)

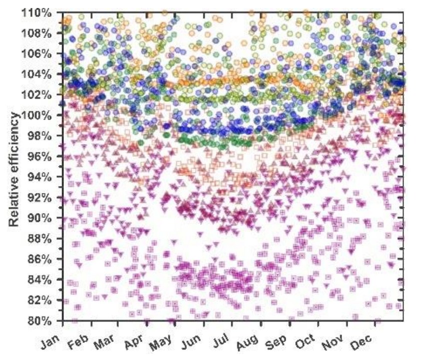

Canada-Montreal (latitude-tilt)

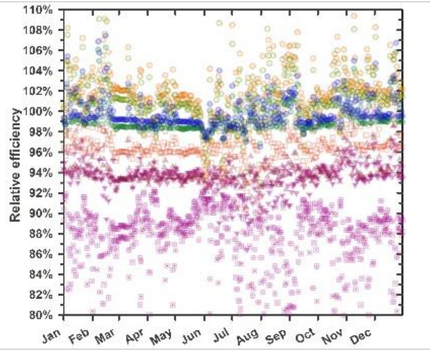

Cabo Verde-Praia (one-axis tracking)

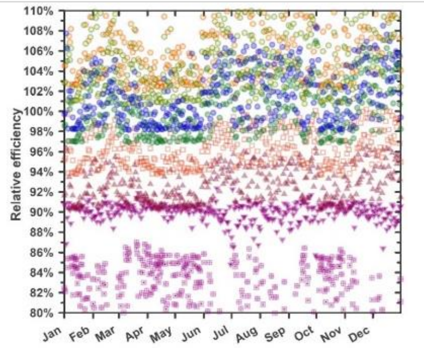

Ecuador-Galapagos (latitude-tilt)

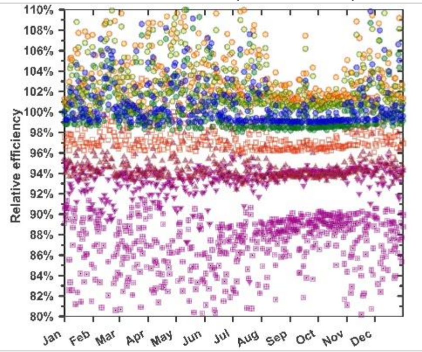

French Guiana-Kourou (one-axis tracking)

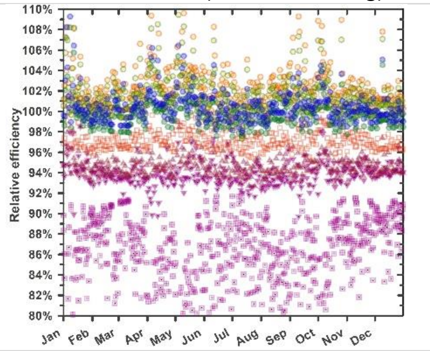

Haiti-Port-au-Prince (one-axis tracking)

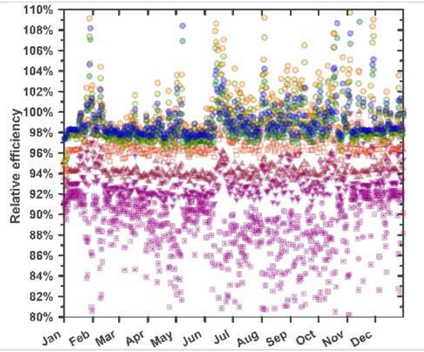

Mexico-Mexico City (one-axis tracking)

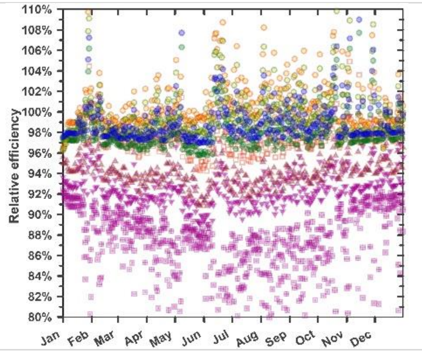

Mexico-Mexico City (latitude-tilt)

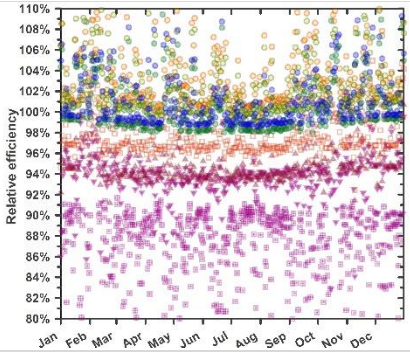

Mexico-Monterrey (one-axis tracking)

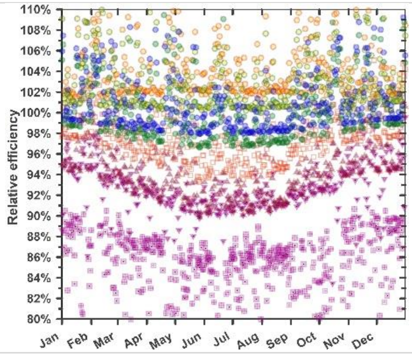

Mexico-Monterrey (latitude-tilt)

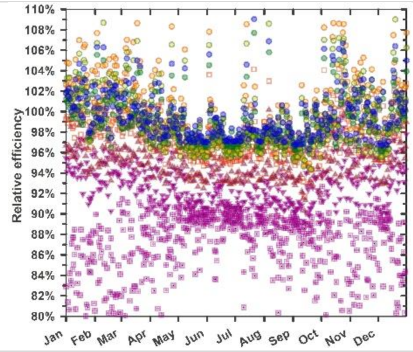

Peru-Cusco (one-axis tracking)

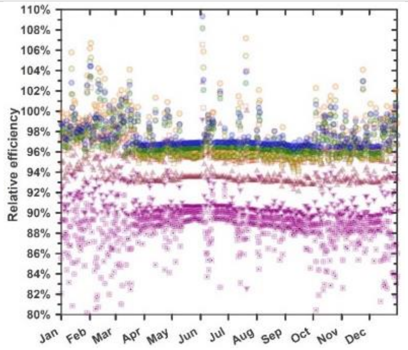

Peru-Puno (one-axis tracking)

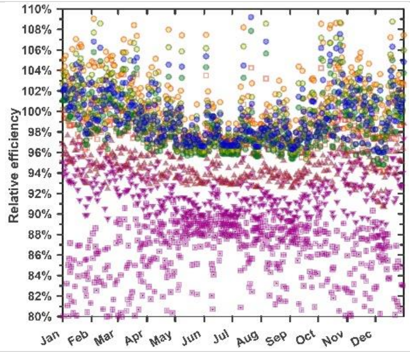

Peru-Puno (latitude-tilt)

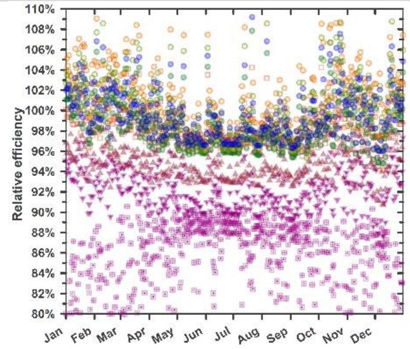

Peru-Cusco (latitude-tilt)

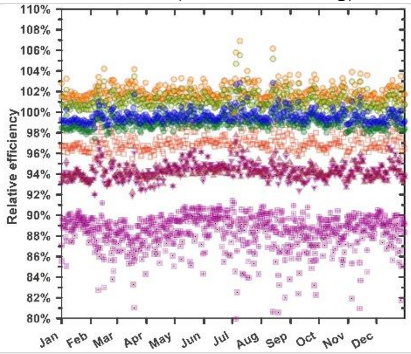

Samoa-Apia (one-axis tracking)

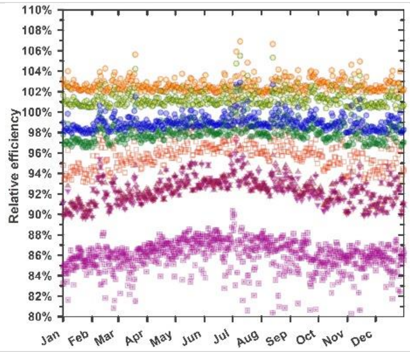

Samoa-Apia (latitude-tilt)

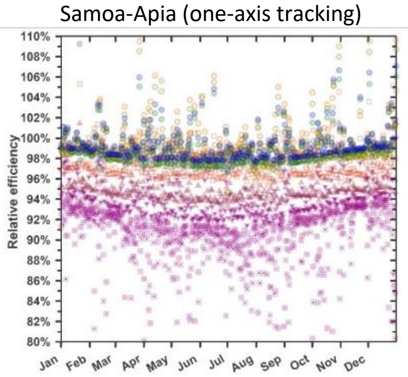

USA-Alamosa (one-axis tracking)

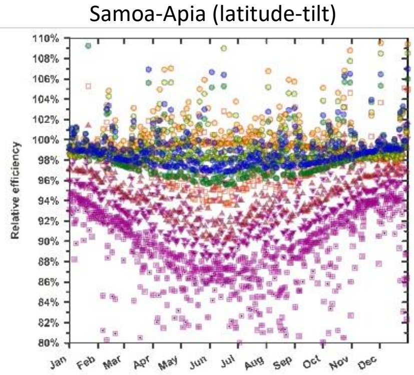

USA-Alamosa (latitude-tilt)

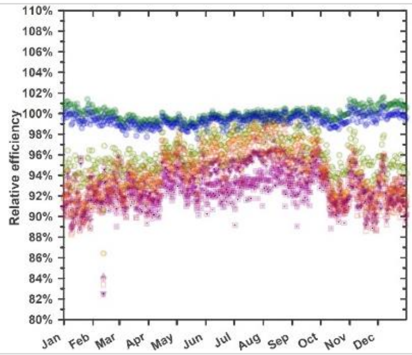

USA-Alamosa (direct normal)

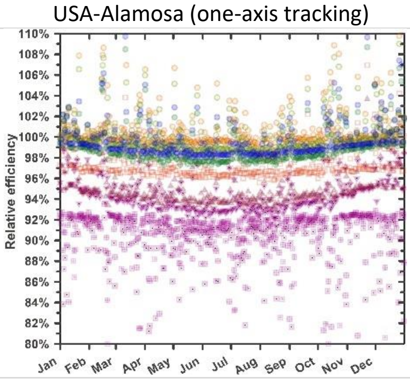

USA-Albuquerque (one-axis tracking)

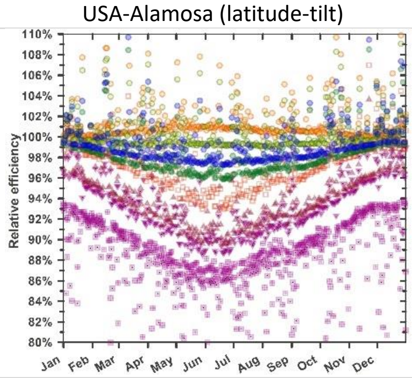

USA-Albuquerque (latitude-tilt)

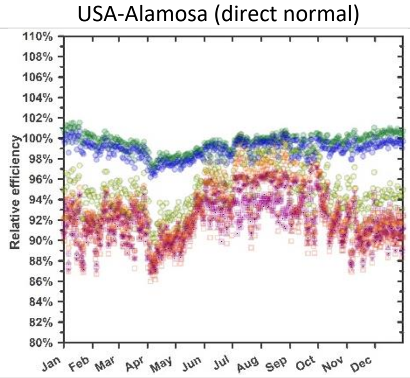

USA-Albuquerque (direct normal)

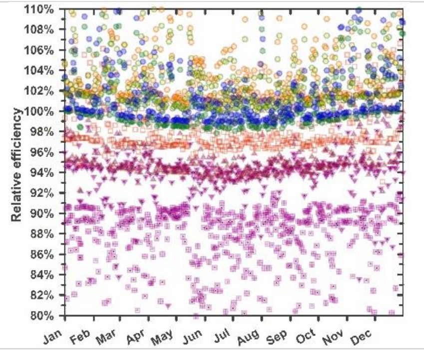

USA-Atlanta (one-axis tracking)

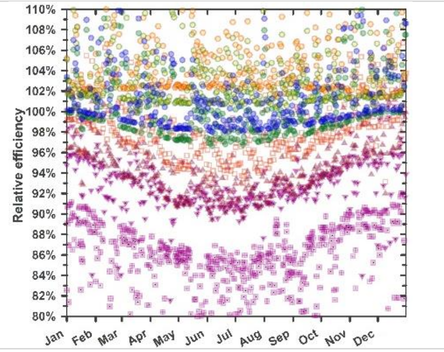

USA-Atlanta (latitude-tilt)

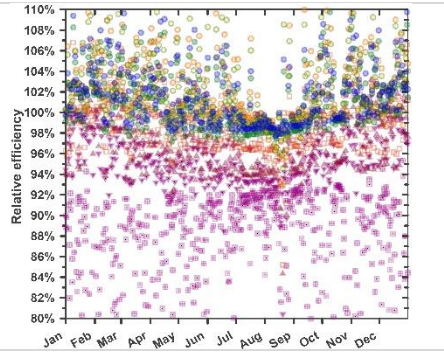

USA-Butte, ID (one-axis tracking)

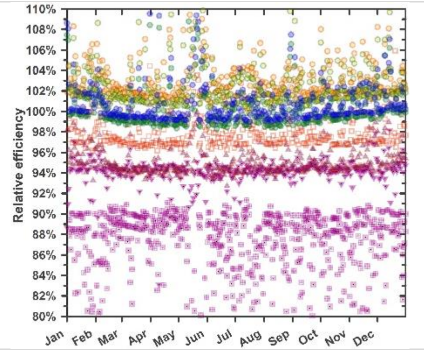

USA-Cocoa, FL (one-axis tracking)

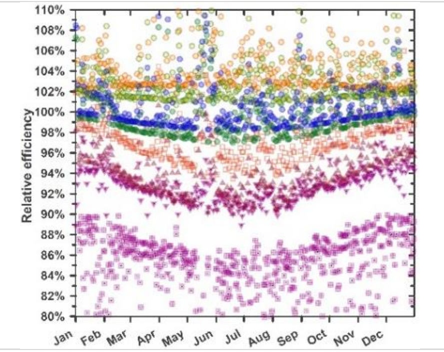

USA-Cocoa, FL (latitude-tilt)

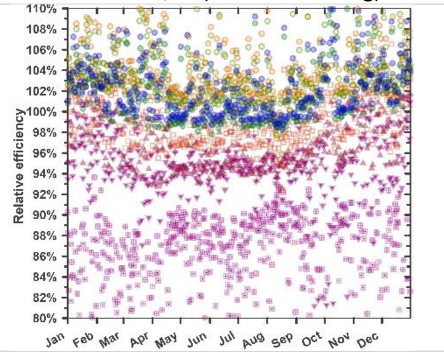

USA-Fargo, ND (one-axis tracking)

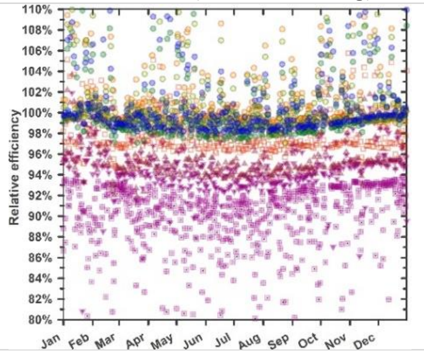

USA-Denver (one-axis tracking)

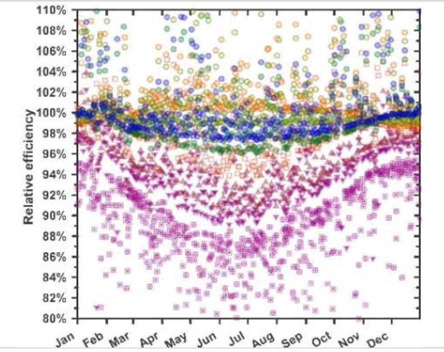

USA-Denver (latitude-tilt)

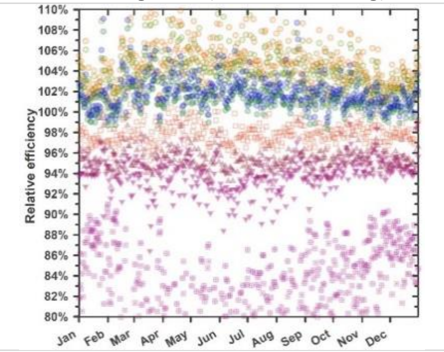

USA-Kona (one-axis tracking)

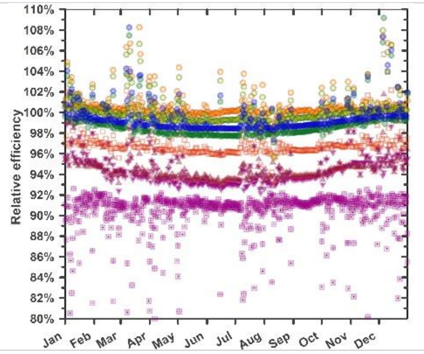

USA-Joshua Tree (one-axis tracking)

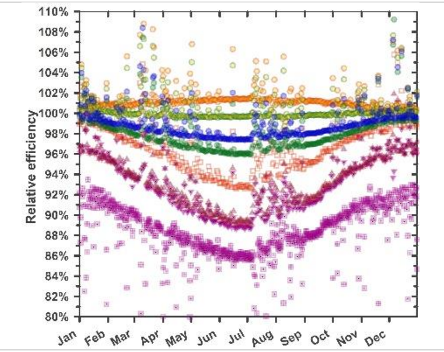

USA-Joshua Tree (latitude-tilt)

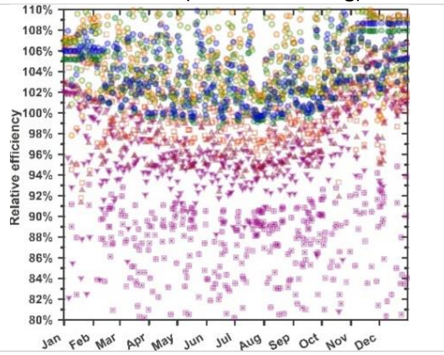

USA-Ketchikan (one-axis tracking)

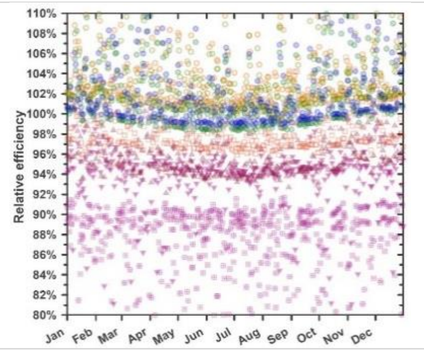

USA-Kansas City (one-axis tracking)

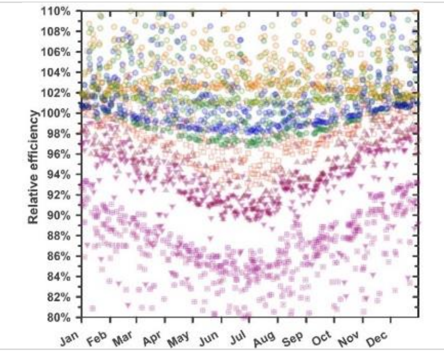

USA-Kansas City (latitude-tilt)

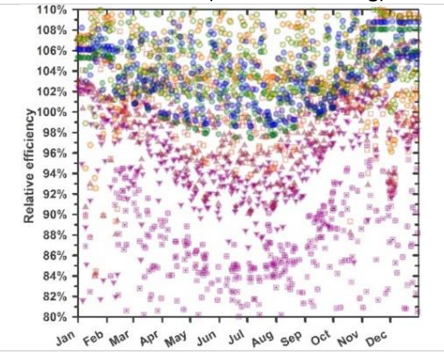

USA-Ketchikan (latitude-tilt)

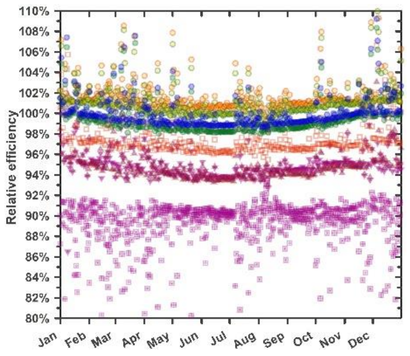

USA-Las Vegas (one-axis tracking)

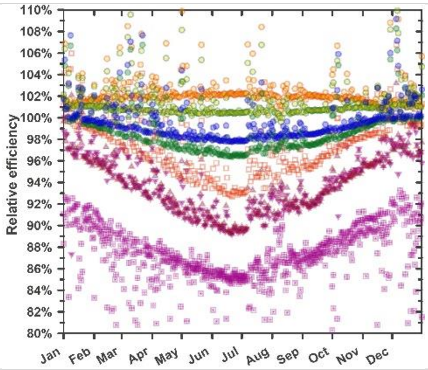

USA-Las Vegas (latitude-tilt)

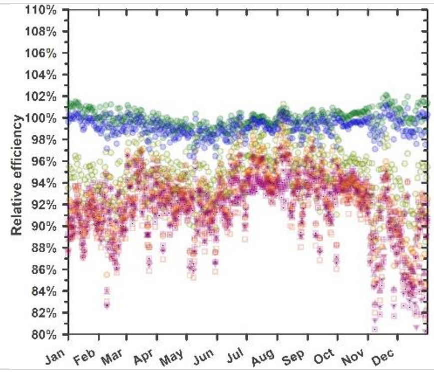

USA-Las Vegas (direct normal)

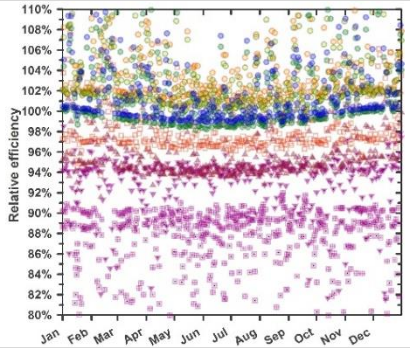

USA-Little Rock (one-axis tracking)

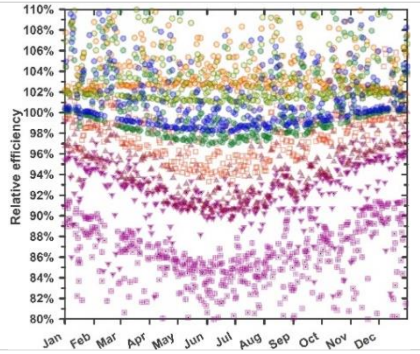

USA-Little Rock (latitude-tilt)

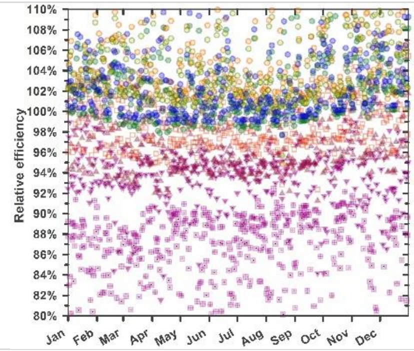

USA-Rochester, MN (one-axis tracking)

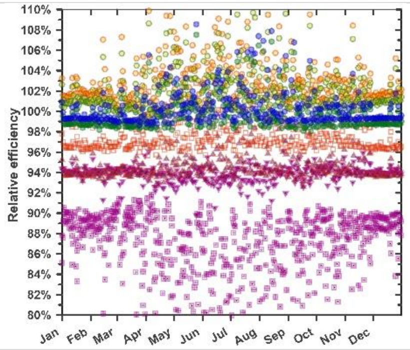

Venezuela-Apure (one-axis tracking)

Daily variation under global operating spectra: silicon and cadmium telluride

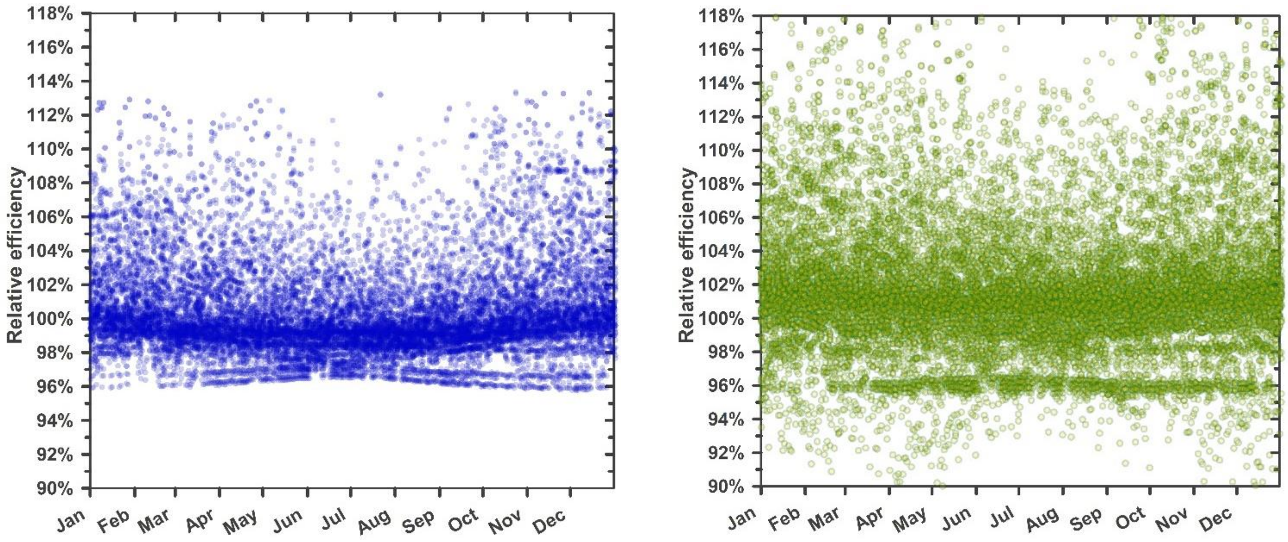

(a) (b)

Fig. E.8. Daily relative efficiencies of (a) silicon and (b) cadmium telluride cells under global operating spectra (25° C) for the sites in Table E.4.

High irradiance on South American highland plateaus

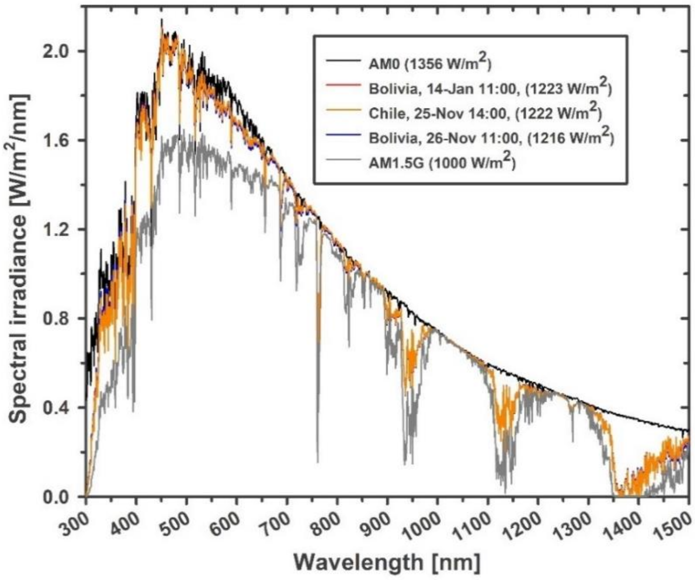

Fig. E.9. The three highest hourly irradiances in the data catalog, obtained for Uyuni, Bolivia and Putre, Chile. Amplitudes are normalized to AM0 at 1050 nm.

References

Air Transport Action Group, 2020. Facts & figures [WWW Document]. URL https://www.atag.org/facts-figures.html (accessed 10.11.20).

Alonso-Abella, M., Chenlo, F., Nofuentes, G., Torres-Ramírez, M., 2014. Analysis of spectral effects on the energy yield of different PV (photovoltaic) technologies: The case of four specific sites. Energy. https://doi.org/10.1016/j.energy.2014.01.024

Amillo, A.M.G., Huld, T., Vourlioti, P., Müller, R., Norton, M., 2015. Application of satellite-based spectrally-resolved solar radiation data to PV performance studies. Energies. https://doi.org/10.3390/en8053455

ASTM E490-00a, 2014. Standard Solar Constant and Zero Air Mass Solar Spectral Irradiance Tables, ASTM International.

ASTM G173-03, 2013. Standard Tables for Reference Solar Spectral Irradiances : Direct Normal and. Astm.

ASTM G173-03, 2012. G173-03(2012) Standard Tables for Reference Solar Spectral Irradiances: Direct Normal and Hemispherical on 37° Tilted Surface, ASTM International.

Boeing, 2020. Boeing: 787 Dreamliner [WWW Document]. URL http://www.boeing.com/commercial/787/ (accessed 10.11.20).

Cornaro, C., Andreotti, A., 2013. Influence of Average Photon Energy index on solar irradiance characteristics and outdoor performance of photovoltaic modules. Prog. Photovoltaics Res. Appl. https://doi.org/10.1002/pip.2194

Dirnberger, D., Blackburn, G., Müller, B., Reise, C., 2015. On the impact of solar spectral irradiance on the yield of different PV technologies. Sol. Energy Mater. Sol. Cells. https://doi.org/10.1016/j.solmat.2014.09.034

Faine, P., Kurtz, S.R., Riordan, C., Olson, J.M., 1991. The influence of spectral solar irradiance variations on the performance of selected single-junction and multijunction solar cells. Sol. Cells. https://doi.org/10.1016/0379-6787(91)90027-M

Fernandez, E.F., Cruz, F.A., Mallick, T.K., Sundaram, S., 2015. Effect of Spectral Irradiance Variations on the Performance of Highly Efficient Environment-Friendly Solar Cells. IEEE J. Photovoltaics. https://doi.org/10.1109/JPHOTOV.2015.2434593

Fernández, E.F., Siefer, G., Schachtner, M., García Loureiro, A.J., Pérez-Higueras, P., 2012. Temperature coefficients of monolithic III-V triple-junction solar cells under different spectra and irradiance levels, in: AIP Conference Proceedings. https://doi.org/10.1063/1.4753865

First Solar, 2020. First Solar [WWW Document]. Tech. Doc. URL http://www.firstsolar.com/Resources/Technical-Documents (accessed 10.11.20).

Foster, V., Bedrosyan, D., 2014. Understanding CO2 Emissions from the Global Energy Sector. Live wire.

Fraunhofer ISE, 2020. Fraunhofer ISE-Power Measurements [WWW Document]. URL https://www.ise.fraunhofer.de/en/rd-infrastructure/accredited-labs/testlab-pv-modules/power-measurements.html (accessed 10.11.20).

Futscher, M.H., Ehrler, B., 2017. Modeling the Performance Limitations and Prospects of Perovskite/Si Tandem Solar Cells under Realistic Operating Conditions. ACS Energy Lett. https://doi.org/10.1021/acsenergylett.7b00596

Gottschalg, R., Betts, T.R., Williams, S.R., Sauter, D., Infield, D.G., Kearney, M.J., 2004. A critical appraisal of the factors affecting energy production from amorphous silicon photovoltaic arrays in a maritime climate. Sol. Energy. https://doi.org/10.1016/j.solener.2004.06.015

Green, M.A., Dunlop, E.D., Hohl-Ebinger, J., Yoshita, M., Kopidakis, N., Hao, X., 2020a. Solar cell efficiency tables (version 56). Prog. Photovoltaics Res. Appl. https://doi.org/10.1002/pip.3303

Green, M.A., Dunlop, E.D., Hohl-Ebinger, J., Yoshita, M., Kopidakis, N., Ho-Baillie, A.W.Y., 2020b. Solar cell efficiency tables (Version 55). Prog. Photovoltaics Res. Appl. https://doi.org/10.1002/pip.3228

Green, M.A., Dunlop, E.D., Levi, D.H., Hohl-Ebinger, J., Yoshita, M., Ho-Baillie, A.W.Y., 2019. Solar cell efficiency tables (version 54). Prog. Photovoltaics Res. Appl. https://doi.org/10.1002/pip.3171

Green, M.A., Emery, K., 1993. Solar cell efficiency tables. Prog. Photovoltaics Res. Appl. https://doi.org/10.1002/pip.4670010104

Green, M.A., Emery, K., Hishikawa, Y., Warta, W., Dunlop, E.D., 2015. Solar cell efficiency tables (Version 45). Prog. Photovoltaics Res. Appl. https://doi.org/10.1002/pip.2573

Green, M.A., Emery, K., Hishikawa, Y., Warta, W., Dunlop, E.D., 2013. Solar cell efficiency tables (version 42). Prog. Photovoltaics Res. Appl. https://doi.org/10.1002/pip.2404

Green, M.A., Hishikawa, Y., Warta, W., Dunlop, E.D., Levi, D.H., Hohl-Ebinger, J., Ho-Baillie, A.W.H., 2017. Solar cell efficiency tables (version 50). Prog. Photovoltaics Res. Appl. https://doi.org/10.1002/pip.2909

Gueymard, C.A., 1995. SMARTS2: a simple model of the atmospheric radiative transfer of sunshine: algorithms and performance assessment. Rep. No. FSEC-PF-270-95.

Gueymard, C.A., Myers, D., Emery, K., 2002. Proposed reference irradiance spectra for solar energy systems testing. Sol. Energy. https://doi.org/10.1016/S0038-092X(03)00005-7

Habte, A., Sengupta, M., Lopez, A., 2017. Evaluation of the National Solar Radiation Database (NSRDB Version 2): 1998-2015. Nrel/Tp-5D00-67722.

Huld, T., Gracia Amillo, A.M., 2015. Estimating PV module performance over large geographical regions: The role of irradiance, air temperature, wind speed and solar spectrum. Energies. https://doi.org/10.3390/en8065159

IEC 60904-9, 2006. IEC 60904-9 Photovoltaic devices – Part 9: Solar simulator performance requirements Dispositifs, 61010-1 © Iec:2001.

IEC 61215-1, 2016. IEC 61215-1-1 Terrestrial photovoltaic (PV) modules – Design qualification and type approval – Part 1-1: Special requirements for testing of crystalline silicon photovoltaic (PV) modules. Int. Electrotech. Comm.

IEC 61853-2, 2016. IEC 61853-2 Photovoltaic (PV) module performance testing and energy rating Part 2: Spectral response, incidence angle and module operating temperature measurements, IEC.

Ishii, T., Otani, K., Takashima, T., Xue, Y., 2013. Solar spectral influence on the performance of photovoltaic (PV) modules under fine weather and cloudy weather conditions. Prog. Photovoltaics Res. Appl. https://doi.org/10.1002/pip.1210

Jinko Solar, 2020. LIMITED WARRANTY.

Jošt, M., Lipovšek, B., Glažar, B., Al-Ashouri, A., Brecl, K., Matič, G., Magomedov, A., Getautis, V., Topič, M., Albrecht, S., 2020. Perovskite Solar Cells go Outdoors: Field Testing and Temperature Effects on Energy Yield. Adv. Energy Mater. https://doi.org/10.1002/aenm.202000454

Kinsey, G.S., 2015. Spectrum sensitivity, energy yield, and revenue prediction of PV modules. IEEE J. Photovoltaics. https://doi.org/10.1109/JPHOTOV.2014.2370256

Kinsey, G.S., Bagienski, W., Nayak, A., Liu, M., Gordon, R., Garboushian, V., 2013. Advancing efficiency and scale in CPV Arrays. IEEE J. Photovoltaics. https://doi.org/10.1109/JPHOTOV.2012.2227992

Kinsey, G.S., Hebert, P., Barbour, K.E., Krut, D.D., Cotal, H.L., Sherif, R.A., 2008. Concentrator multifunction solar cell characteristics under variable intensity and temperature. Prog. Photovoltaics Res. Appl. https://doi.org/10.1002/pip.834

Lee, M., Ngan, L., Hayes, W., Panchula, A.F., 2015. Comparison of the effects of spectrum on cadmium telluride and monocrystalline silicon photovoltaic module performance, in: 2015 IEEE 42nd Photovoltaic Specialist Conference, PVSC 2015. https://doi.org/10.1109/PVSC.2015.7356174

Lufthansa, 2020. Boeing 787-9.

Marzo, A., Beiza, F., Ferrada, P., Alonso, J., Roman, R., 2017. Comparison of Atacama Desert Solar Spectrum vs. ASTM G173-03 Reference Spectra for Solar Energy Applications. https://doi.org/10.18086/eurosun.2016.09.01

Minemoto, T., Nagae, S., Takakura, H., 2007. Impact of spectral irradiance distribution and temperature on the outdoor performance of amorphous Si photovoltaic modules. Sol. Energy Mater. Sol. Cells. https://doi.org/10.1016/j.solmat.2007.02.012

Monokroussos, C., Bliss, M., Qiu, Y.N., Hibberd, C.J., Betts, T.R., Tiwari, A.N., Gottschalg, R., 2011. Effects of spectrum on the power rating of amorphous silicon photovoltaic devices. Prog. Photovoltaics Res. Appl. https://doi.org/10.1002/pip.1080

Myers, D.R., Emery, K., Gueymard, C., 2004. Revising and validating spectral irradiance reference standards for photovoltaic performance evaluation. J. Sol. Energy Eng. Trans. ASME. https://doi.org/10.1115/1.1638784

Myers, D.R., Emery, K., Gueymard, C., 2002. Revising and validating spectral irradiance reference standards for photovoltaic performance evaluation, in: International Solar Energy Conference. https://doi.org/10.1115/SED2002-1074

Myers, D.R., Gueymard, C.A., 2004. Description and availability of the SMARTS spectral model for photovoltaic applications, in: Organic Photovoltaics V. https://doi.org/10.1117/12.555943

Nann, S., Emery, K., 1992. Spectral effects on PV-device rating. Sol. Energy Mater. Sol. Cells. https://doi.org/10.1016/0927-0248(92)90083-2

NREL, 2020. Best Research-Cell Efficiency Chart | Photovoltaic Research | NREL [WWW Document]. URL https://www.nrel.gov/pv/cell-efficiency.html (accessed 10.12.20).

NREL, 2010. Typical Meteorological Year 3 [WWW Document]. Natl. Sol. Radiat. Data Base.

Peters, I.M., Buonassisi, T., 2018. Energy Yield Limits for Single-Junction Solar Cells. Joule. https://doi.org/10.1016/j.joule.2018.03.009

Philipps, S.P., Peharz, G., Hoheisel, R., Hornung, T., Al-Abbadi, N.M., Dimroth, F., Bett, A.W., 2010. Energy harvesting efficiency of III-V triple-junction concentrator solar cells under realistic spectral conditions. Sol. Energy Mater. Sol. Cells. https://doi.org/10.1016/j.solmat.2010.01.010

Reynolds, S., Smirnov, V., 2015. Modelling Performance of Two- and Four-terminal Thin-film Silicon Tandem Solar Cells under Varying Spectral Conditions, in: Energy Procedia. https://doi.org/10.1016/j.egypro.2015.12.321

Schweiger, M., 2015. Impact of spectral irradiance on energy yield of PV modules measured in different climates. 4th PV Perform. Model. Monit. 17 Work. https://doi.org/10.13140/RG.2.2.33591.73122

Sengupta, M., Xie, Y., Lopez, A., Habte, A., Maclaurin, G., Shelby, J., 2018. The National Solar Radiation Data Base (NSRDB). Renew. Sustain. Energy Rev. https://doi.org/10.1016/j.rser.2018.03.003

Simon, M., Meyer, E.L., 2011. The effects of spectral evaluation of c-Si modules. Prog. Photovoltaics Res. Appl. https://doi.org/10.1002/pip.973

Solar Frontier, 2020. Solar Frontier [WWW Document]. URL https://www.solar-frontier.com/eng/support/index.html (accessed 10.11.20).

SunPower, 2020. SunPower [WWW Document]. Products. URL https://us.sunpower.com/products/solar-panels (accessed 10.11.20).

Xie, Y., Sengupta, M., 2018. A Fast All-sky Radiation Model for Solar applications with Narrowband Irradiances on Tilted surfaces (FARMS-NIT): Part I. The clear-sky model. Sol. Energy. https://doi.org/10.1016/j.solener.2018.09.056

Xie, Y., Sengupta, M., Wang, C., 2019. A Fast All-sky Radiation Model for Solar applications with Narrowband Irradiances on Tilted surfaces (FARMS-NIT): Part II. The cloudy-sky model. Sol. Energy. https://doi.org/10.1016/j.solener.2019.06.058

Ye, J.Y., Reindl, T., Aberle, A.G., Walsh, T.M., 2014. Effect of solar spectrum on the performance of various thin-film PV module technologies in tropical Singapore. IEEE J. Photovoltaics. https://doi.org/10.1109/JPHOTOV.2014.2328585